https://doi.org/10.5194/egusphere-2025-2255
Preprint. Discussion started: 2 June 2025

Urban pollution monitoring with the AOTF-based NO_2 camera: validation with other DOAS instruments

Pierre Gramme[1,*], Cedric Busschots[1,*], Emmanuel Dekemper[1,*], Didier Pieroux[1], Noel Baker[1], Stefano Casadio[2], Anna Maria Iannarelli[2], Nicola Ferrante[2], Annalisa Di Bernardino[3], Paolo Pettinari[4], Elisa Castelli[4], Luca di Liberto[5], and Francesco Cairo[5]

[1]Royal Belgian Institute for Space Aeronomy, Ringlaan 3, 1180 Ukkel, Belgium
[2]Serco Italia S.p.A., Via Bernardino Alimena 111-119, 00173 Rome, Italy
[3]Sapienza University of Rome, Physics Department, Piazzale A. Moro 5, 00185 Rome, Italy
[4]National Research Council (CNR), Institute of Atmospheric Sciences and Climate (ISAC), Via Piero Gobetti 101, 40129 Bologna, Italy
[5]National Research Council (CNR), Institute of Atmospheric Sciences and Climate (ISAC), Via Fosso del Cavaliere 100, 00133 Rome, Italy
[*]These authors contributed equally to this work.

Correspondence: Pierre Gramme (pierre.gramme@aeronomie.be) and Cedric Busschots (cedric.busschots@aeronomie.be)

Abstract. Elevated surface concentrations of nitrogen dioxide (NO_2) are associated with poor air quality, making its detection and monitoring important for human health and the environment. Existing instruments such as the TROPOMI satellite currently deliver daily global maps of NO_2 tropospheric columns, and the future Sentinel–4 instrument will return hourly maps; while areas of strong concentrations (cities, large industries) can be detected in these satellite observations, their spatio-temporal resolution remains too coarse to capture local hot spots and quick variations.

In the context of urban air quality monitoring, we present a new type of remote sensing instrument capable of observing spatial and temporal gradients in the NO_2 field which is not currently possible with either space instruments or from the routine operations of conventional diffraction grating and other ground-based remote sensing instruments. This novel instrument is based on an acousto-optical tunable filter (AOTF) located at the heart of a telecentric imaging system. The instrument acquires spectral images in the region 430–455 nm, where NO_2 exhibits strong absorption features. A dense spectral sampling was commanded in order to enable the application of the DOAS method (differential optical absorption spectroscopy) in the processing of the spectra measured by each detector pixel.

In March 2024, the instrument was deployed at the BAQUNIN supersite for atmospheric research, located in the center of Rome. In order to validate the NO_2 camera measurements, coincident acquisitions by a MAX-DOAS and a Pandora spectrometer were performed. The results show very good agreement among the three instruments. They also illustrate the additional capabilities of the NO_2 camera in observing the spatial and temporal variability of the urban NO_2 field.

https://doi.org/10.5194/egusphere-2025-2255
Preprint. Discussion started: 2 June 2025

1 Introduction

Humans are directly exposed to the chemical composition of Earth's boundary layer, the lowest part of the troposphere where emissions from the surface are mixing. In that layer, the nitrogen oxides (NOx) family is made of nitrogen oxide (NO) and nitrogen dioxide (NO_2), the former being primarily released in combustion processes (both natural or anthropogenic) while the latter is produced by reaction of NO with ozone (O_3) or hydroperoxy radical (HO_2). Through photolysis, NO_2 can be converted back into NO, such that a photochemical equilibrium persists most of the day. Among other effects, high levels of NO_x are associated with poor air quality, given the role of the molecule in the advent of photochemical smog episodes (Seinfeld and Pandis, 2006).

Of these NO_x compounds, nitrogen dioxide (NO_2) is the most important for human health (World Health Organization, 2021). There is scientific evidence that chronic exposure to NO_2 can cause emphysema (Last et al., 1994) and that, together with ozone, it increases oxidative stress in the small airways within the lungs (Morrow, 1984). Long-term exposure to ambient NO_2 is found to be correlated with increased mortality (Chen et al., 2024; Huangfu and Atkinson, 2020).

This negative influence on human health prompted the World Health Organization (WHO) to release Air Quality Guidelines, updated in 2021, and more recently translated into a European law (Directive 2022/0347). While European Union Member States are required to deploy air sampling stations, with some guidelines on the number of stations and their location, the Directive fails to address the problem of the large variation of exposure by citizens living in different neighborhoods of close proximity. Such large differences have been observed in citizen science projects, such as the *CurieuzenAir/CurieuzeNeuzen* experiment, in which thousands of sampling flasks have been deployed in both Brussels (Lauriks et al., 2022) and Flanders (De Craemer et al., 2020). The WHO identifies this inadequate monitoring of spatial variations in the concentration of pollutants such as NO_2 as one of the main gaps in the global coverage of air pollution monitoring (World Health Organization, 2021). These spatial and temporal differences are especially pronounced in urban environments.

In recent years, several new remote sensing instruments have been developed that attempt to capture the variability of the NO_2 field with a high spatial and temporal resolution (Lohberger et al., 2004; Heue et al., 2008; Dekemper et al., 2016; Peters et al., 2019; Mettepenningen et al., 2024). This paper discusses the improvements made to the instrument in (Dekemper et al., 2016) and the results obtained with this instrument during a validation campaign in Rome.

2 The improved AOTF-based NO_2 camera

The AOTF-based NO_2 camera concept stems from the ALTIUS instrument, an ESA satellite mission for the monitoring of the stratospheric O_3 layer which relies on the acquisition of spectral images of the atmospheric limb at selected wavelengths (Fussen et al., 2019). As part of the ALTIUS mission pre-developments, a proof-of-concept optical breadboard of its VIS channel was produced and tested in the laboratory. Although not meant to leave the laboratory, its potential for imaging NO_2 plumes was recognized and tested during the AROMAT–II campaign (Merlaud et al., 2020). That version of the instrument as well as the results of the campaign were fully described in (Dekemper et al., 2016).

https://doi.org/10.5194/egusphere-2025-2255
Preprint. Discussion started: 2 June 2025

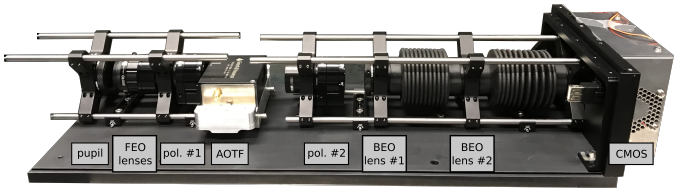

Figure 1. The current optics setup is made with commercial off-the-shelf components.

The instrument being reported here is an improved version of the original breadboard in almost every aspect, from basic parameters such as reduced size and mass, to its improved optical performance and acquisition software (see section 2.1). While its raw data remain as monochromatic images stacked in hypercubes, when compared to the AROMAT campaign operations, many more wavelengths are now acquired in routine operations in order to achieve higher accuracy.

In the next section, we describe the instrument, its operating scheme, and the raw data it produces. In the following section, we discuss the main differences between this instrument and the conventional diffraction grating-based spectrometers which are currently used to monitor the field of NO_2 as part of operational networks.

2.1 Instrument description

The fundamental instrumental concept described in (Dekemper et al., 2012) and (Dekemper et al., 2016) has been kept: a telecentric front-end module captures the light and sends it on to the AOTF. Upon crossing the crystal, a narrow band of the incident light spectrum experiences a coupling with the acoustic beam created in the crystal by a piezo-electric transducer. The acousto-optic interaction diffracts the selected part of the spectrum into another direction, such that two beams leave the AOTF: one containing photons of the same energy (the monochromatic beam), and the other containing the rest of the spectrum (the white beam). The back-end optics only captures the diffracted beam, which forms the monochromatic image on the detector. The selection of another wavelength happens by tuning the acoustic wave frequency. Fig. 1 shows a picture of the optomechanical system. The fundamental physics of acousto-optic interaction in birefringent crystals is described in (Harris and Wallace, 1969; Chang, 1974). Further details on telecentric systems using AOTFs can be found in, e.g. (Suhre et al., 2004), and a discussion on the optimization of AOTF parameters used for spectral imaging applications is provided in (Voloshinov et al., 2007).

One of the most significant improvements concerns the field of view (FOV) which was increased to $23° \times 23°$ by reducing the focal length of the telecentric lens. The size of the back-end optics was also reduced by using shorter focal lengths. As a consequence, the instrument is now much more compact and can be manipulated by a single person. The electronics (RF generation and amplification, single-board computer) fit in a separate box. For the validation campaign, a pan-and-tilt head was used to control the pointing of the instrument (EKO sun tracker with GPS receiver). The optics, electronics, and pointing modules have all been placed on a tripod. The camera housing was redesigned to withstand adverse weather; the optics are sealed off from the outside, while the cooled detector is partially outside this sealed environment, so that fresh air can reach

https://doi.org/10.5194/egusphere-2025-2255
Preprint. Discussion started: 2 June 2025

Figure 2. The NO_2 camera and the two reference instruments installed for the campaign at the BAQUNIN-APL supersite.

the cooling block of the Peltier element. Figure 2 shows the exterior of the camera and its surrounding environment during the campaign.

Table 1 details the specifications of the original versus the newer version of the NO_2 camera.

	Original (Dekemper et al., 2016)	This work
Size of optics channel	1 m	40 cm
Mass	40 kg	6 kg
FoV	$5.8° \times 5.8°$	$23° \times 23°$
AOTF	Gooch & Housego model TF625-350-2-12-BR1A	Gooch & Housego model TF625-350-2-12-BR1A
Spectral range	430 – 450 nm	400 – 490 nm
Detector	Princeton Instrument Pixis 512B CCD	ZWO ASI2600MM Pro CMOS
ADC	16 bits	16 bits
Read noise	5 e^- rms	<1.4 e^- rms
# pixels	512x512	6248x4176 (binned to 512x512)
Pixel area	24x24 μm^2	3.76x3.76 μm^2 (binned to 30x30 μm^2)
Per-pixel FoV	0.011° x 0.011°	0.045° x 0.045° (binned)
Full well	$3 \cdot 10^5$ e^-	$5 \cdot 10^4$ e^- (binned to $3.2 \cdot 10^6$ e^-)
Pointing control	elevation (manual)	azimuth and elevation with EKO STR-21G

Table 1. Comparison of the original and current versions of the NO_2 camera.

The software reliability was tackled with newly designed control software that runs on an ARM-based single board computer. An OKdo Rock 5B with 8GB RAM was selected for this purpose. It accepts an NVMe M.2 SSD to temporarily store the acquired images. It is responsible for the synchronized operation of the detector, RF electronics, and EKO. At night, the raw measurement data are transferred automatically to storage servers over the internet.

https://doi.org/10.5194/egusphere-2025-2255
Preprint. Discussion started: 2 June 2025

Central wavelength	400 nm	430 nm	460 nm	490 nm
FWHM	1.0 nm	1.1 nm	1.7 nm	2.5 nm

Table 2. Instrument's spectral resolution (width of Gaussian kernel) as a function of the wavelength. A linear interpolation is performed between the values shown here.

2.2 Spectral response function

The instrument's spectral response function (SRF) is approximated by a variable-width Gaussian convolution scheme, where the full width at half maximum (FWHM) of the kernel evolves as a function of the central wavelength, as shown in Table 2. These choices were made from fitting the convolved theoretical solar spectrum (Chance and Kurucz, 2010) to the measured intensity at zenith during a calibration experiment. The merit function for the fit was the mean absolute difference between both spectra, after taking their logarithm and subtracting a low-order polynomial approximation from each.

2.3 Data acquisition

The image projected on the CMOS detector is roughly square. Of the full rectangular native resolution of 6248×4176 pixels, only a square region of interest of 4096 by 4096 pixels is selected. The resulting image is then binned in two steps. A first 4×4 binning is executed by the detector itself, then the software bins the image again, leading to a final resolution of 512 by 512 pixels. The main motivation for binning is the increase of the signal-to-noise ratio (SNR) by a factor 8. This is required given the target variability of about 1% to be detected in the signal intensity while keeping the per-frame exposure time at 1000 ms. As positive side-effects, the frame rate is also increased, and the data storage needs are reduced. The gain parameter was chosen to be high enough to minimize the read noise and quantization noise and low enough to avoid saturation.

The wavelength band that is sampled for the NO_2 measurements ranges from 427 to 454.9 nm. This includes many strong spectral features as will be shown hereunder in Fig. 6. Every 0.15 nm an image is taken. This sampling ensures compliance with the Nyquist criterion, as the spectral resolution of the filter is not smaller than 0.7 nm, expressed as the FWHM of the SRF. In total, this amounts to 188 distinct spectral images forming a hyperspectral cube (or simply a cube). An additional image is acquired at the start of every cube. This image is taken with the AOTF off (0 W of RF power injected into the transducer), which therefore only contains the instrument stray light. In the data processing, this stray light image can be used to remove the stray light from all the other spectral images. Each of the images includes metadata about the scene location, time, and camera and pointing parameters.

During a complete acquisition, the instrument is first pointed in the direction of the scene of interest using the EKO. Then, one or multiple cubes of the scene are acquired, followed by a cube acquired while the instrument points at the zenith. These zenith cubes are needed to remove the solar spectrum and the stratospheric signal during the data analysis. A flow chart of the complete acquisition scheme is shown in Fig. 3.

https://doi.org/10.5194/egusphere-2025-2255
Preprint. Discussion started: 2 June 2025

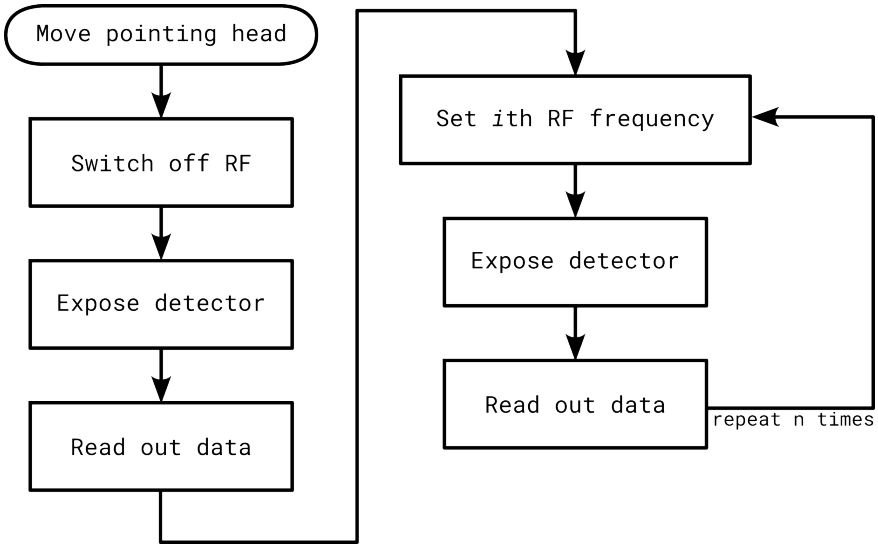

Figure 3. Schematic representation of the acquisition process for a single *hypercube*. For every acoustic frequency *n*, the corresponding RF frequency *i* needs to be set.

2.4 Main differences with grating-based instruments

The goal of the NO_2 camera is to go a step further in terms of the observing capability of the small-scale spatial structures and the high temporal variability of the NO_2 field emanating from distributed sources of a city. These new observing capabilities should be assessed with respect to the performance of operational remote sensing instruments, such as the MAX-DOAS instruments of the Network for the Detection of Atmospheric Composition Change (NDACC) research infrastructure (Van Roozendael et al., 2024), or the Pandora spectrometers of the Pandonia Global Network (Herman et al., 2009).

The MAX-DOAS and the Pandora instruments are diffraction grating spectrometers that measure the UV-VIS solar light which is either scattered by the atmosphere or directly transmitted. The former method yields more freedom with respect to the observation directions, as potentially any pair of azimuth and elevation angle can be targeted. Some instrument designs can also sample a range of azimuth or elevation angles in one single acquisition (e.g., see Peters et al. (2019)). In that case, a 1-D NO_2 field can be observed.

When an image of a scene is desirable, this method can be expanded to two dimensions by sweeping the 1-D field of view along the second dimension of the scene (Lohberger et al., 2004; Heue et al., 2008; Peters et al., 2019; Mettepenningen et al., 2024). However, a limitation of this method is the loss of temporal consistency between the different slices of the scene, especially when observing dynamic features such as plumes (Platt et al., 2014).

The NO_2 camera uses a different method to create images of the NO_2 field. Instead of scanning the scene, (Dekemper et al., 2016) proposed to capture complete images of the scene, but one wavelength at a time. The imaging quality is that of a real imaging system, offering a higher spatial sampling than fiber-bundled based diffraction grating spectrometers, while temporal

https://doi.org/10.5194/egusphere-2025-2255
Preprint. Discussion started: 2 June 2025

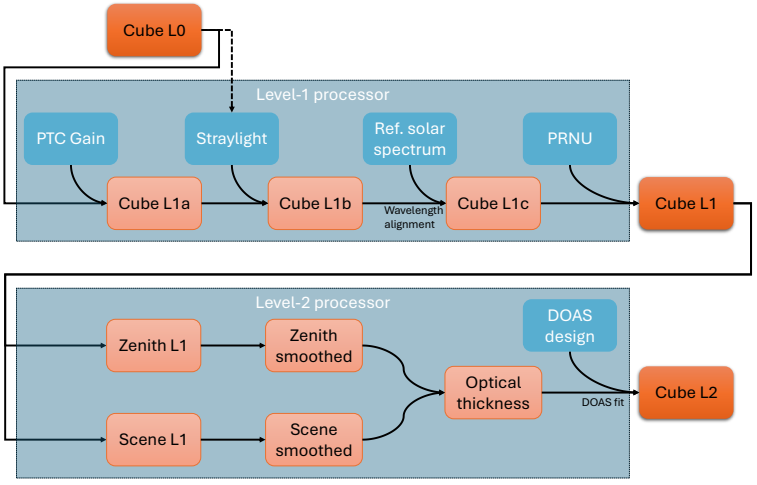

Figure 4. Overview of the data processing for the retrieval of NO_2 dSCDs (Level-2 data) from the NO_2 camera acquisitions (Level-0 data).

variations can still be tracked in successive images. One drawback lies in the perturbations caused by the spectra recorded by pixels which have seen objects moving during the cube acquisitions. Additionally, the optical throughput of a telecentric AOTF-based imager is lower than that of a diffraction grating spectrometer, yielding a lower signal-to-noise ratio.

On the other hand, this method has the advantage that images are acquired from the start. Pointing errors are easily corrected by using features in the pictures. More importantly, highly dynamic processes can be detected and monitored, especially when the camera is focusing on a limited number of wavelengths. Whereas diffraction grating-based systems automatically record the complete spectrum for their design bandwidth, AOTF-based systems allow the user to cherry-pick the wavelengths of interest: there is no fixed sequence of wavelengths required. Therefore, a wavelength band of interest can be defined for any species, and only this wavelength band will be sampled by the camera. This way, the amount of images required can be decreased, reducing the time necessary for a single scene measurement.

3 NO_2 camera data processing

3.1 Overview

The data processing for the NO_2 camera is organized into Level-0 (raw spectra), Level-1 (calibrated spectra) and Level-2 (retrieval outcome). The main processing steps are shown in Fig. 4, and more details are provided in the next sections.

3.2 Level-1 Processor

The first step of the Level-1 processor (L1P) is to convert the acquired raw data from digital number to electron count. A preliminary calibration experiment was performed in order to compute a photon transfer curve (PTC) and derive its parameters,

https://doi.org/10.5194/egusphere-2025-2255
Preprint. Discussion started: 2 June 2025

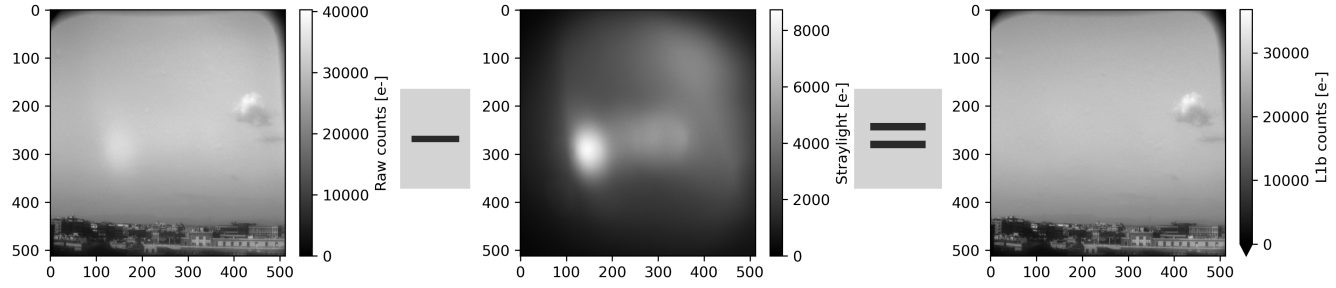

Figure 5. Illustration of stray light removal. Note the smaller values in the color scale for the central image, which was captured with the AOTF turned off.

following Janesick (2007). At gain parameter 200 (×0.1 dB), used during the campaign, our computations gave a gain of 0.0793 e^-/DN, a read noise of 1.206 e^-, and a fixed pattern noise (FPN) of 0.2%, confirming the vendor characteristics. The PTC showed that the CMOS detector's response is very close to linear, so that the conversion to electrons amounts to a simple multiplication by the gain (and a detector offset which can be ignored thanks to the following stray light removal). The stray light images (acquired at least once per hyperspectral cube) are also converted to electrons (e^-), and subtracted pixel by pixel from the target images. To maintain physical interpretability, all values under 1 e^- are forced to 1 e^- (i.e. close to the read noise).

An illustration of this stray light removal is shown in Fig. 5. The intensity of stray light observed is typically less than 10% of the scene intensity, except in a small region of about 70×70 pixels. This region changes slightly depending on pointing and solar angles, and its stray light may reach values comparable to the real stray light-corrected intensity (especially on scenes with less light in their lower part, and at wavelengths under 435 nm).

The optical wavelength filtered by the AOTF at a given acoustic frequency is known to depend on the crystal temperature. Although this variation can be computed and corrected for, a more precise wavelength registration is obtained by detecting the Fraunhofer lines, which are clearly visible in the measured spectra. For this purpose, the average intensity at the 64×64 central pixels of the cube is compared to the convolved solar reference spectrum, same as in Section 2.2. The wavelength correction function is the solution of a non-linear optimization problem whose search space consists of all increasing affine functions of the wavelength, with the identity function as the start point. The score which is minimized is the mean absolute difference of logarithms, after subtracting broadband differences as in Section 2.2.

The final step in Level-1 processing is to correct for pixel response non-uniformity (PRNU), a type of instrumental bias where some pixels would show a different sensitivity from others when exposed to the same input signal. For simplicity, we model the PRNU with a per-pixel scaling factor independent of the wavelength, even though this hypothesis may not be correct. Note that the first step of Level-2 data processing (see below) is to compute the ratio between the zenith and scene intensities. Therefore, regardless of the choice of linear scaling used in the PRNU correction, it will not have any impact on the level 2

https://doi.org/10.5194/egusphere-2025-2255
Preprint. Discussion started: 2 June 2025

product. That correction can thus be considered as a cosmetic step.

Putting it all together, the Level-1 intensity in electrons I_{L1} at wavelength λ and pixel i, j is computed as:

$$I_{\mathrm{L1}}(\lambda, i, j) = \frac{\max\left(1\ ,\ G\ S(\tilde{\lambda}, i, j) - G\ S_0(i, j)\right)}{\mathrm{PRNU}(i, j)}, \tag{1}$$

where

- $\tilde{\lambda}$ is the nominal wavelength, before alignment;
- λ is the truly measured wavelength after alignment: $\lambda = \tilde{\lambda} + \Delta(\tilde{\lambda})$, where Δ is a smooth function of the nominal wavelength optimizing the alignment of Fraunhofer structure;
- G is the detector's gain;
- S is the L0 signal intensity in digital numbers;
- S_0 is the L0 stray light signal intensity in digital numbers (i.e. with AOTF off);
- I_{L1} is the Level-1 signal intensity in electrons;
- $\mathrm{PRNU}(i, j)$ is the PRNU factor.

In addition to the calibrated light intensity, a pointing map is computed as well, assigning an elevation and azimuth viewing angle to each pixel of the Level-1 image. This map is calibrated using prominent features, such as buildings and mountains, whose viewing angles were determined from publicly available topographic maps and/or aerial photos. Its precision is expected around 0.05° (one pixel).

3.3 Level-2 Processor

The retrieval of NO_2 differential slant column densities (dSCDs) from hyperspectral cubes is based on the well established DOAS method (Differential Optical Absorption Spectroscopy, see (Platt and Stutz, 2008)), which relies on the Beer–Lambert law:

$$I(\lambda) = I_0(\lambda) \cdot \exp\left(-\sum_{k=1}^{K} S^k(\lambda) c_k\right), \tag{2}$$

where

- $I(\lambda)$ is the measured spectrum of interest, after extinction in the atmosphere,
- $I_0(\lambda)$ is the zenith spectrum, an approximation of the spectrum at the top of the atmosphere,
- $S^k(\lambda)$ is the absorption cross-section of the species k, depending on wavelength $[\mathrm{cm}^2/\mathrm{molec}]$,
- c_k is the dSCD of the species k $[\mathrm{molec}/\mathrm{cm}^2]$.

The principle of the DOAS method is to focus on high-frequency spectral structures in this equation, approximating the low-frequency structures (such as instrumental effects, aerosol scattering, etc.) with a low-order polynomial $P_{\leq n}(\lambda) = \sum_k p_k \lambda^k$.

https://doi.org/10.5194/egusphere-2025-2255
Preprint. Discussion started: 2 June 2025

Parameter	NO_2 **camera**	**MAX-DOAS**	**Pandora**
Wavelength range	427–454 nm	434–455 nm	435–490 nm
Solar reference	Chance and Kurucz (2010)		
Reference spectra	Fixed reference, zenith on Mar–21 16:03 UTC		Smallest elevation angle
Intensity offset	None	Linear, degree$\leq$1	Linear, degree$\leq$1
Low-order polynomial	Degree $\leq$4	Degree $\leq$5	Degree $\leq$4
Cross-sections:			
– NO_2 (294 K)	Vandaele et al. (1998)		
– Water vapour	HITRAN2012 — Rothman et al. (2013)		
– O_3 (223 K)	Serdyuchenko et al. (2014)		
– O_4 (293 K) (O_2 dimer)	Finkenzeller and Volkamer (2022)	Thalman and Volkamer (2013)	Hermans et al. (1999)
– Ring effect pseudo-absorber	Wagner et al. (2009)		

Table 3. Parameters and cross-sections used for the DOAS retrieval for each smoothed pixel of the NO2 camera measurements

Defining the optical thickness $\tau(\lambda)$ as the log-ratio, the previous equation becomes:

$$\tau(\lambda) \equiv \log \frac{I_0(\lambda)}{I(\lambda)} = \sum_{k=0}^{n} p_k \lambda^k + \sum_{k=1}^{K} S^k(\lambda) c_k. \tag{3}$$

Writing $\{\lambda_l\}_{l=1\ldots L}$ for the wavelengths at which the optical thickness was measured, and defining the DOAS design matrix as

$$A \equiv \begin{pmatrix} 1 & \lambda_1 & \cdots & \lambda_1^n & S^1(\lambda_1) & \cdots & S^K(\lambda_1) \\ 1 & \lambda_2 & \cdots & \lambda_2^n & S^1(\lambda_2) & \cdots & S^K(\lambda_2) \\ \vdots & \vdots & \vdots & \vdots & \vdots & \vdots & \vdots \\ 1 & \lambda_L & \cdots & \lambda_L^n & S^1(\lambda_L) & \cdots & S^K(\lambda_L) \end{pmatrix} \in \mathbb{R}^{L\times(1+n+K)}, \tag{4}$$

Equation 3 can be rewritten as a simple linear fit for each pixel (i, j):

$$A \cdot \boldsymbol{x}(i,j) = \boldsymbol{\tau}(i,j) \;\; \forall i,j, \tag{5}$$

whose unknown $\boldsymbol{x}(i,j)$ are the concatenation of the polynomial coefficients $\boldsymbol{p}(i,j)$ and the dSCDs $\boldsymbol{c}(i,j)$ at pixel (i,j).

For the NO_2 camera, the value of the measured response (optical thickness $\boldsymbol{\tau}(i,j)$), and of these unknown variables $\boldsymbol{x}(i,j)$ will vary from pixel to pixel, while the design matrix A is common to all pixels. As noted earlier, the per-pixel FoV is around 0.045°. In order to make it comparable to the reference instruments ($\sim$0.3×1° for MAX-DOAS and $\sim$1.5×1.5° for Pandora), a box smoothing is applied to the zenith and the scene using a uniform 7×23 or 33×33 pixels kernel on each Level-1 intensity map, before computing the optical thickness.

The DOAS fitting settings are summarized in Table 3 and an example of retrieval output is shown in Fig. 6.

https://doi.org/10.5194/egusphere-2025-2255
Preprint. Discussion started: 2 June 2025

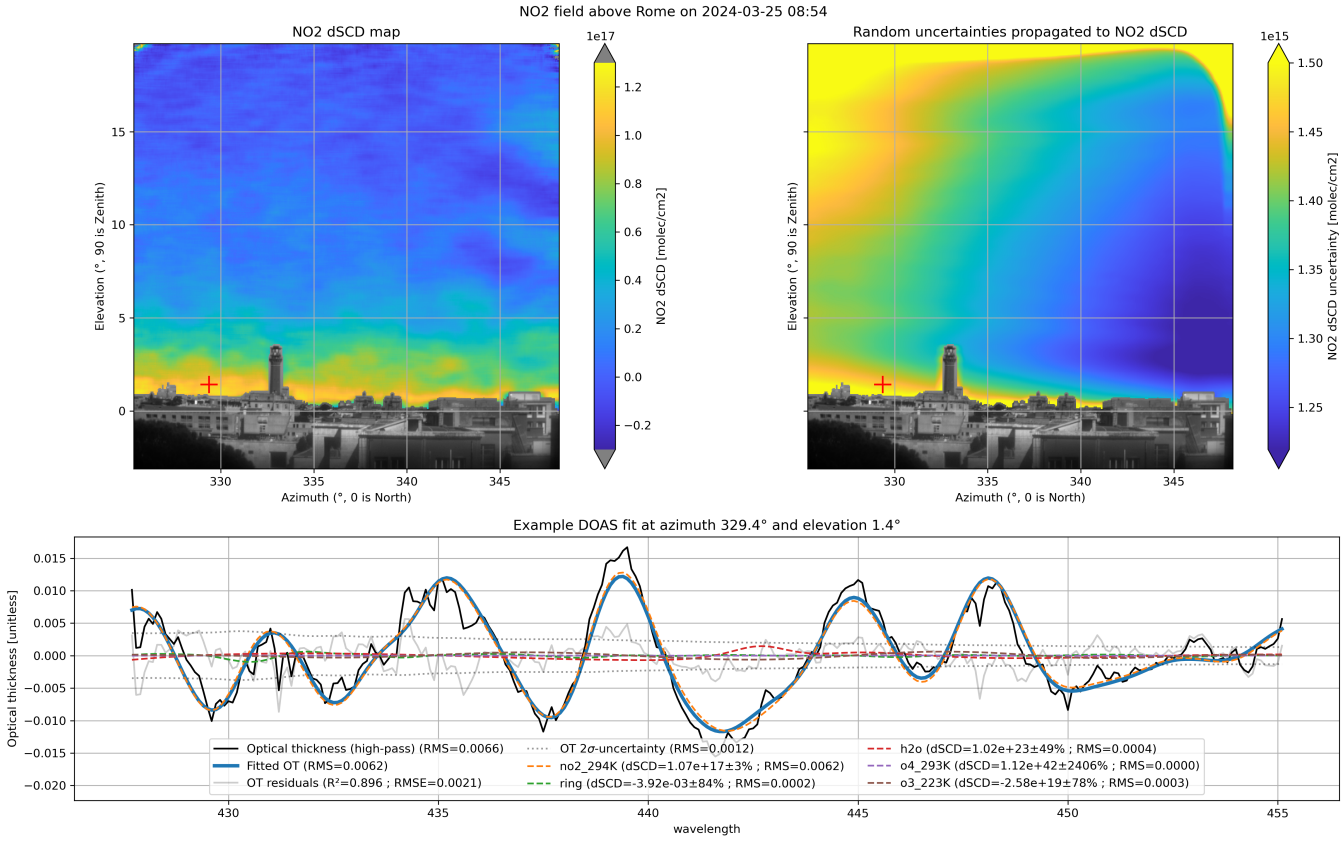

Figure 6. Example of output from NO_2 camera retrieval, acquired in Rome on March 25, from 8:55 to 9:01 UTC. The top left panel shows the map of NO_2 dSCDs retrieved for each pixel, while the top right panel shows its estimated uncertainties. In order to give finer spatial context, the pixels under the horizon for both images show the landscape (from the Level-1 data at 455 nm). The bottom panel shows the details of the DOAS fit for one example pixel, marked with a red cross in the top images.

3.4 Characterization of Uncertainties

Considering the NO2 dSCD as the measurand, we characterize the uncertainty on its estimated values by uncertainty propagation through the measurement model described in the previous sections, starting at its input quantities. In a first attempt, only the random uncertainty in the intensity measurements is considered.

The main random uncertainties affecting the signal (Level-1) measurements come from the CMOS sensor. Following the PTC analysis mentioned earlier, three independent noise components are considered: the read noise, the Poisson shot noise, and the fixed pattern noise. The uncertainty associated with a CMOS output of s electrons is then

$$u_{\mathrm{CMOS}}(s) = \sqrt{\sigma_{\mathrm{RN}}^2 + s + p_{\mathrm{FPN}}^2 s^2},$$

https://doi.org/10.5194/egusphere-2025-2255
Preprint. Discussion started: 2 June 2025

where σ^2_{RN}=0.6 e^- is the variance of the read noise, s is the variance of the Poisson shot noise, and p_{FPN}=0.2% is the proportion of FPN. This is valid for the target images as well as the stray light images. At the typical values of input signal (i.e. 5,000 to 60,000 e^-), the read noise is negligible compared to shot noise, so we ignore it for the sake of simplicity. As for the FPN, its maximal contribution is obtained when the input signal is highest. For an input of 60,000 e^-, the uncertainty including 0.2% FPN amounts to 273 e^- vs 245 e^- without FPN, which proves that the FPN impact is limited or even negligible depending on the signal level. Moreover, the subtraction of stray light and the division by the PRNU map in Equation 1 have the side effect of removing the additive and the multiplicative components of FPN, respectively. Potentially remaining FPN would be much smaller and come from non-linear effects which are hard to characterize. For this reason, FPN is also ignored, and the standard uncertainty of the Level-1 signal is

$$u_{\mathrm{L1}}(\lambda,i,j) \simeq \frac{1}{\mathrm{PRNU}(i,j)}\sqrt{G\,S(\tilde{\lambda},i,j) + G\,S_0(i,j)}.$$

While we do expect close values of $I_{\mathrm{L1}}(\lambda,i,j)$ for neighboring wavelengths and pixels, we assume that their measurement errors are statistically independent. Therefore, we do not consider the covariance structure among the measurement errors at different pixels and wavelengths in the signal. We also hypothesize that the target and zenith cubes are independent. We are aware of the limiting aspect of these assumptions: we will address them in future developments, and an empirical approach is proposed for the campaign results presented in this work. Propagating these random uncertainties in the definition of optical thickness (including the preliminary box-smoothing intensities with size $k \times k$) gives

$$u_\tau(\lambda,i,j) = \sqrt{\frac{u^2_{\mathrm{L1}}(\lambda,i,j)}{k^2 I^2_{\mathrm{L1}}(\lambda,i,j)} + \frac{u^2_{z,\mathrm{L1}}(\lambda,i,j)}{k^2 I^2_{z,\mathrm{L1}}(\lambda,i,j)}} \simeq \frac{1}{k}\sqrt{\frac{1}{I_{\mathrm{L1}}(\lambda,i,j)} + \frac{1}{I_{z,\mathrm{L1}}(\lambda,i,j)}}, \tag{6}$$

where the last approximation is valid when the stray light intensity is small compared to the target image.

Assuming that the DOAS design matrix A is perfectly known, the uncertainty on $\boldsymbol{\tau}(x,y)$ propagates to the dSCDs and polynomial coefficients as the following covariance matrix:

$$\Sigma_{\boldsymbol{x}(i,j)} = \left(A^\top \,\mathrm{diag}\left(1/\boldsymbol{u}^2_{\boldsymbol{\tau}}(i,j)\right)\, A\right)^{-1}. \tag{7}$$

Returning the full covariance structure for each pixel is not practical for the data users, therefore only the square root of the diagonal terms is reported:

$$\boldsymbol{u}_{\boldsymbol{x}}(i,j) = \sqrt{\mathrm{diag}\left(\Sigma_{\boldsymbol{x}(i,j)}\right)}. \tag{8}$$

This produces a one-dimensional uncertainty estimate for the NO_2 dSCD at each pixel, which we can display in a map similarly to the dSCDs themselves, as shown in Fig. 6. The residuals of the DOAS spectral fit show some non-random structure and are regularly larger than the estimated uncertainty on optical thickness. This shows that our estimation underestimates the true total uncertainty, which was expected because we ignored the systematic contributions.

https://doi.org/10.5194/egusphere-2025-2255
Preprint. Discussion started: 2 June 2025

4 Campaign in Rome

4.1 Objectives

The goal of the measurement campaign in Rome is to validate the correctness of the NO_2 camera retrievals with two state-of-the-art remote sensing instruments: a Pandora and a MAX-DOAS, described hereafter.

In Rome, the Atmospheric Physics Laboratory (APL) of Sapienza University hosts the BAQUNIN super site (Boundary-layer Air Quality-analysis Using Network of INstruments), where several ground-based instruments are available that monitor the boundary layer air quality (Iannarelli et al., 2022). This urban observatory is equipped to host ground-based instruments such as the NO_2 camera for inter-comparison/inter-calibration campaigns. It was selected as location for a first urban test campaign in a challenging environment showing strong spatial and temporal variations.

4.2 Reference NO_2 remote sensing instruments

4.2.1 MAX-DOAS

The MAX-DOAS instrument used for the campaign is a SkySpec-2D system by Airyx. This system has been acquired by CNR-ISAC in 2021 and operated from the CIRAS (CNR Isac Rome Atmospheric obServatory), in the CNR research area of Tor Vergata since September 2021. The instrument is composed of a telescope (installed outdoors), a spectrometer unit, and a measurement PC. The spectrometer is connected to the telescope via an optical fiber. The spectrometer unit contains two spectrometers that simultaneously acquire the spectra in the UV and VIS spectral ranges at a high spectral resolution. The prism telescope covers elevation angles from -10° to 190°. The 2D model allows the user to measure at different azimuth angles.

The instrument was transferred from CIRAS to BAQUNIN and installed on the roof of APL, on another platform about 5 meters away and lower than the Pandora and NO2 camera. The measurements were analyzed using QDOAS software and the same parameters as in (Pettinari et al., 2022). These parameters are summarized in Table 3 for convenience.

4.2.2 Pandora

Pandora-2S instruments are fiber-fed hyperspectral spectrometers mounted on a microprocessor-controlled azimuth/elevation tracker and manufactured by SciGlob LLC (Elkridge, MD, USA). They are regrouped in the Pandonia Global Network (PGN), which is co-funded by NASA and ESA and operated by LuftBlick OG (Innsbruck, Austria). The instrument present at the BAQUNIN-APL supersite has identifier PAN#117.

For each day of PAN#117 measurements, a set of level-2 fit files is produced by the PGN centralized processing, each corresponding to a specific measurement mode and target species. Because the campaign focused on NO_2, the “nvh3” data product was analyzed. A detailed description of the fit, its parameters, and its outputs is provided in (Cede et al., 2025) and summarized in Table 3 for convenience. The uncertainty estimates of the retrieved NO_2 dSCDs were obtained by combining in quadrature their independent, structured and common uncertainties.

https://doi.org/10.5194/egusphere-2025-2255
Preprint. Discussion started: 2 June 2025

In order to dSCDs comparable to the NO_2 camera and the MAX-DOAS, the reference spectrum must agree between the different instruments. The NO_2 camera and the MAX-DOAS used a fixed zenith reference acquired on the 21st of March at 16:00 UTC for all of their dSCDs. The Pandora relies on centralized processing to obtain an NO_2 dSCD. This centralized processing requires the use of a sequential reference measurement. Within the Pandonia Global Network, the chosen reference is the spectrum taken at the lowest elevation angle during each azimuthal scan.

The difference in reference between the instruments could be compensated by comparing the Pandora average zenith dSCD during each azimuthal scan with the corresponding retrieval from MAX-DOAS. A correction term was computed for each azimuthal scan and added to all dSCDs in the scan. This correction was also accounted for in the uncertainty estimates.

4.3 Acquisition plan

Four primary azimuth angles were selected for the actual measurement campaign: 27°, 124°, 130°, and 340°. Sample images showing the scenes in the different azimuth directions are shown in Fig. 7. The each different azimuth represents a different type of environment. In the direction of 27° and 340°, the area is mostly residential, whereas 124° and 130° are mixed residential and industrial zones. For the latter azimuth directions, the optical path is limited by the mountains for parts of the image. The tower that is clearly visible in the image taken in the 340° direction was used to calibrate the pointing of each instrument.

After a calibration and test phase in the beginning of the campaign, the Pandora and MAX-DOAS started sampling the NO_2 field inside the field of view of the NO_2 camera. This allows the user to reconstruct a two-dimensional NO_2 dSCD map for each instrument. Figure 7b highlights these sample points for both the MAX-DOAS and Pandora.

In both azimuth and elevation, the Pandora samples every 1°. A denser spatial sampling is not necessary as the field of view of the Pandora is roughly a circle of 1.5° diameter. The MAX-DOAS has a field of view of around 0.3° vertically by 1° horizontally. Therefore, a measurement was taken every 0.5° in elevation angle and every 1° horizontally.

5 Campaign results

5.1 Comparison methodology

For every Pandora and MAX-DOAS measurement, the closest NO_2 camera pixel in space is determined. For this pixel, the dSCD value is compared to the results of the Pandora and MAX-DOAS. Both in azimuth and elevation, a tolerance of 0.1° was allowed. When the pointing correction is applied correctly, the elevation angle and the time difference remain the two parameters that influence the quality of the correlation the most, as we will now discuss.

Figure 8a shows all the dSCDs measured by both the MAX-DOAS and their corresponding dSCD retrieved by the NO_2 camera. For this comparison, a maximum time difference of 30 minutes is allowed between the MAX-DOAS and the NO_2 camera measurement. The different measurement points are colored according to the elevation angle at which they are measured. Ideally, all measured points would lie on the diagonal: both dSCDs would be equal in this case. The dots colored in red indicate elevation angles well below the horizon (-1°). The dots colored in yellow are measurement points between -1° and 1°.

https://doi.org/10.5194/egusphere-2025-2255
Preprint. Discussion started: 2 June 2025

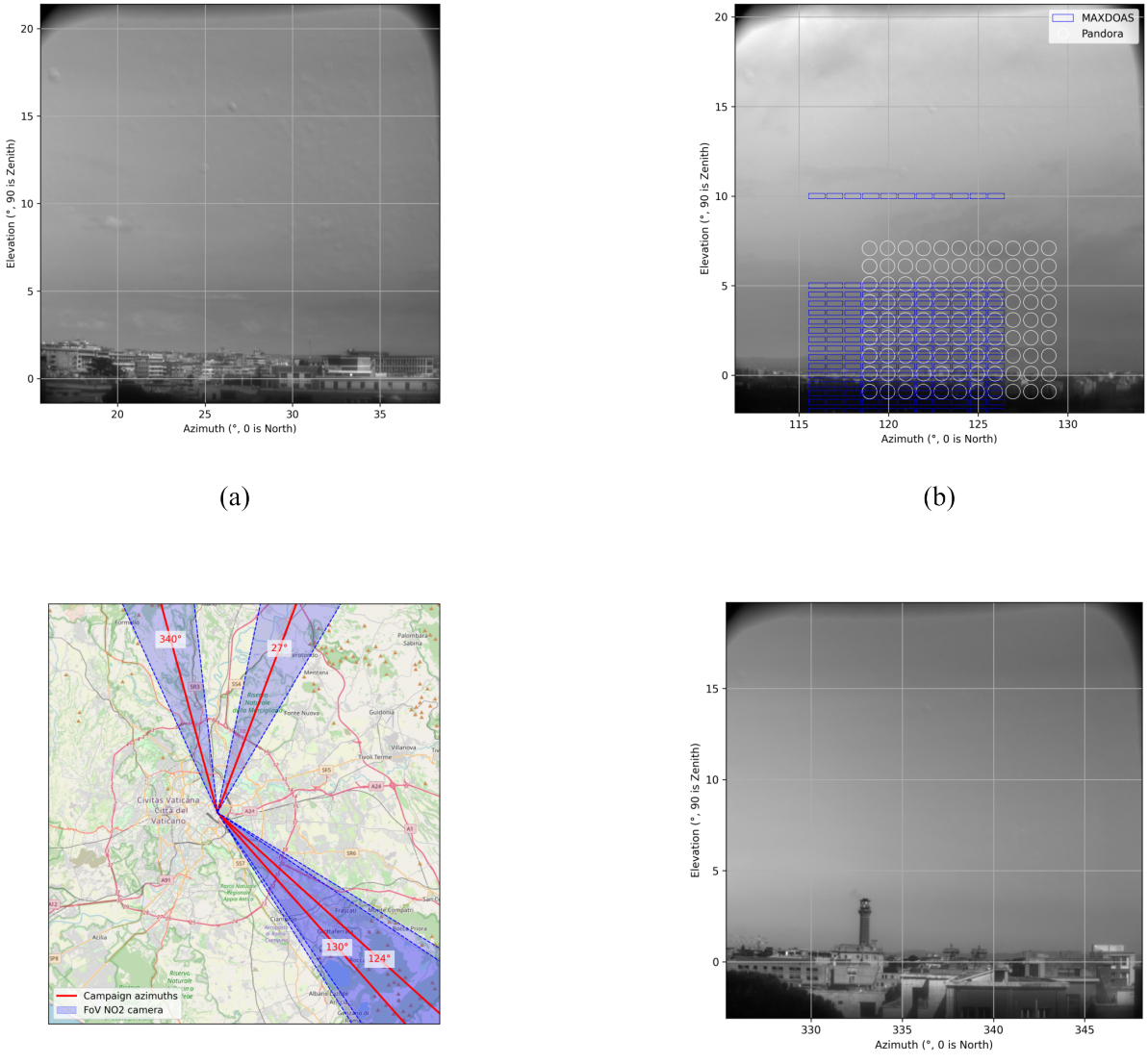

Figure 7. Representative spectral images (at 460 nm) of the main azimuth directions observed during the campaign, with (a) 27°, (b) 124°, and (d) 340° respectively. Each one covers a different type of environment. In addition, panel (b) shows the spatial sampling of the Pandora and MAX-DOAS within the field of view of the NO_2 camera is illustrated. For the sake of readability, this is not shown on the other scenes. Panel (c) shows the four main azimuths used during the measurement campaign. The shaded area in blue shows the field of view of the camera. For 124° and 130°, the camera takes pictures in the direction of 126° and 128° respectively. This allows us to have more comparison points with the other instruments. Map data in Panel (c) © OpenStreetMap contributors, licensed under the Open Database License (ODbL).

https://doi.org/10.5194/egusphere-2025-2255
Preprint. Discussion started: 2 June 2025

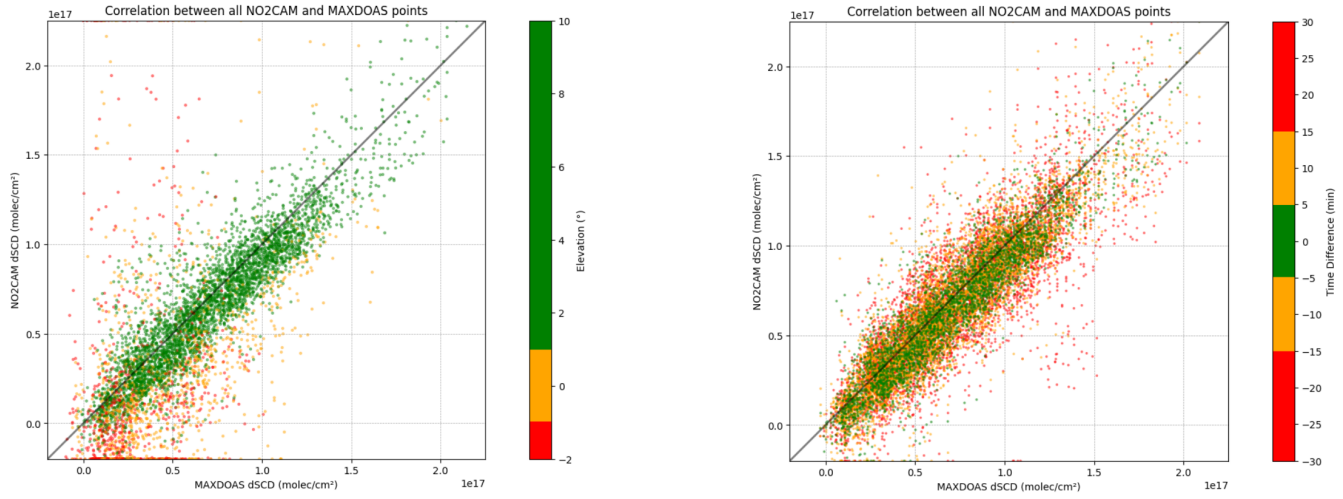

(a) (b)

Figure 8. Comparing dSCDs between the NO_2 camera and the MAX-DOAS shows the strong impact of measurements under the horizon and of large differences in measurement timestamps. Panel (a) shows that the low elevation points differ more significantly from the diagonal than the points above 1° (green versus red). Panel (b) focuses on elevation above 1° and shows that the allowed time difference for the comparison strongly influences the results: smaller time differences have better correspondence (green versus red). In both panes, values outside the viewing window are clipped to the viewing window border.

The green dots show the measurements for elevation angles higher than 1°. Values outside the limits of the axes are clipped to the axis limit. The different colors demonstrate that, for low elevation angles, the correlation between the MAX-DOAS and the NO_2 camera is significantly worse than for higher elevation angles. For the Pandora, the same conclusion holds true (not shown). This is due to the presence of buildings (visible in Fig. 7), their albedo, and the short slant column of NO_2 between them and the instruments. Because the instruments were located a few meters away from each other (including a difference in elevation for the MAX-DOAS), the parallax error leads to differences in the observed scenes. For the remainder of the paper, we will remove from the comparison all points that are at or below 1°.

For Fig. 8a, a maximum of 30 minutes was allowed between the MAX-DOAS and the NO_2 camera measurement. This time difference has a significant impact on the comparison between the instruments. Figure 8b illustrates this influence. Here, only elevation angles above 1° are shown. The less stringent the time requirements become, the more spread out the values are. Values outside the limits of the axes are again clipped to the axis limit. This illustrates that the NO_2 field presents dynamic patterns at the scale of minutes. Therefore, we restrict the time tolerance to ± 5 minutes for the comparisons in this paper.

5.2 Comparison results

A simple difference and a linear regression were used to characterize the relation between the Pandora/MAX-DOAS and the NO_2 camera measurements. The measurement points used for this were those taken within 5 minutes of the NO_2 camera mea-

https://doi.org/10.5194/egusphere-2025-2255
Preprint. Discussion started: 2 June 2025

	vs MAX-DOAS	vs Pandora
Number of observation pairs	3445	785
NO_2 camera bias (mean difference) [$molec/cm^2$]	1.3e14	1.4e14
Root-mean-square error [$molec/cm^2$]	1.4e16	1.4e16
Linear regression		
– Slope (95% CI)	0.99±0.01	0.94±0.03
– Intercept [$molec/cm^2$]	3.1e15	4.3e15
– Coefficient of determination (R^2)	0.85	0.86

Table 4. Summary statistics on the comparison of the Camera's NO_2 dSCDs vs each reference instrument, on all common retrievals from the campaign.

surement at elevation angles higher than 1°. All summary statistics are detailed in Table 4. In particular, the root-mean-square error (RMSE) obtained is 1.4e16 $molec/cm^2$ vs both references. The regression was calculated on all azimuth directions and is shown with the corresponding scatterplot in Fig. 9. Outliers outside the axis limits have been excluded for the regression. The regression slope obtained is 0.99 for the comparison with MAX-DOAS. For Pandora, the slope is 0.94, which is significantly smaller than unity. We attribute this difference to the longer wavelength range used in the Pandora retrievals, which is expected to include photons with a longer optical path, hence mechanically increasing the Pandora's dSCDs.

Finally, a direct comparison between both reference instruments is also included in Fig. 9, using the same filters (time tolerance of 5 minutes, and ignoring points at or below 1° elevation). It shows a RMSE of 7e15 and mean bias of 2e15, and its line of best fit has a slope of 0.99±0.04 and an R^2 value of 0.97. Due to small differences in the scanning schedule of the Pandora and MAX-DOAS, this direct comparison includes only 69 measurement points, much less than the comparisons involving the NO_2 camera. In this direct comparison, we would actually expect a regression slope above 1, but the very limited number of points might have prevented us from observing it, as shown by the larger confidence interval.

5.3 Imaging results

Example images of the dSCDs measured in the different azimuthal directions are shown in Fig. 10. In these figures, fine structures in the NO_2 field can be distinguished. As expected, lines of sight grazing the horizon are capturing much higher NO_2 dSCDs. The imaging quality of the NO_2 camera also reveals horizontal and vertical gradients. An interesting case is, for instance, the enhancement on the left side of Fig. 10b, which should be further investigated. In addition, some figures show artifacts in the upper part of the image. These artifacts are created by the moving clouds, whereas the lower region of the image is left unaffected.

In addition to the quantitative comparison made earlier, a qualitative comparison can also be made with the reference instruments. Figure 11 shows a NO_2 dSCD map taken in the direction of 124°, with overlays showing the corresponding MAX-DOAS and Pandora dSCDs. Similar patterns are found with all three measurement instruments.

https://doi.org/10.5194/egusphere-2025-2255
Preprint. Discussion started: 2 June 2025

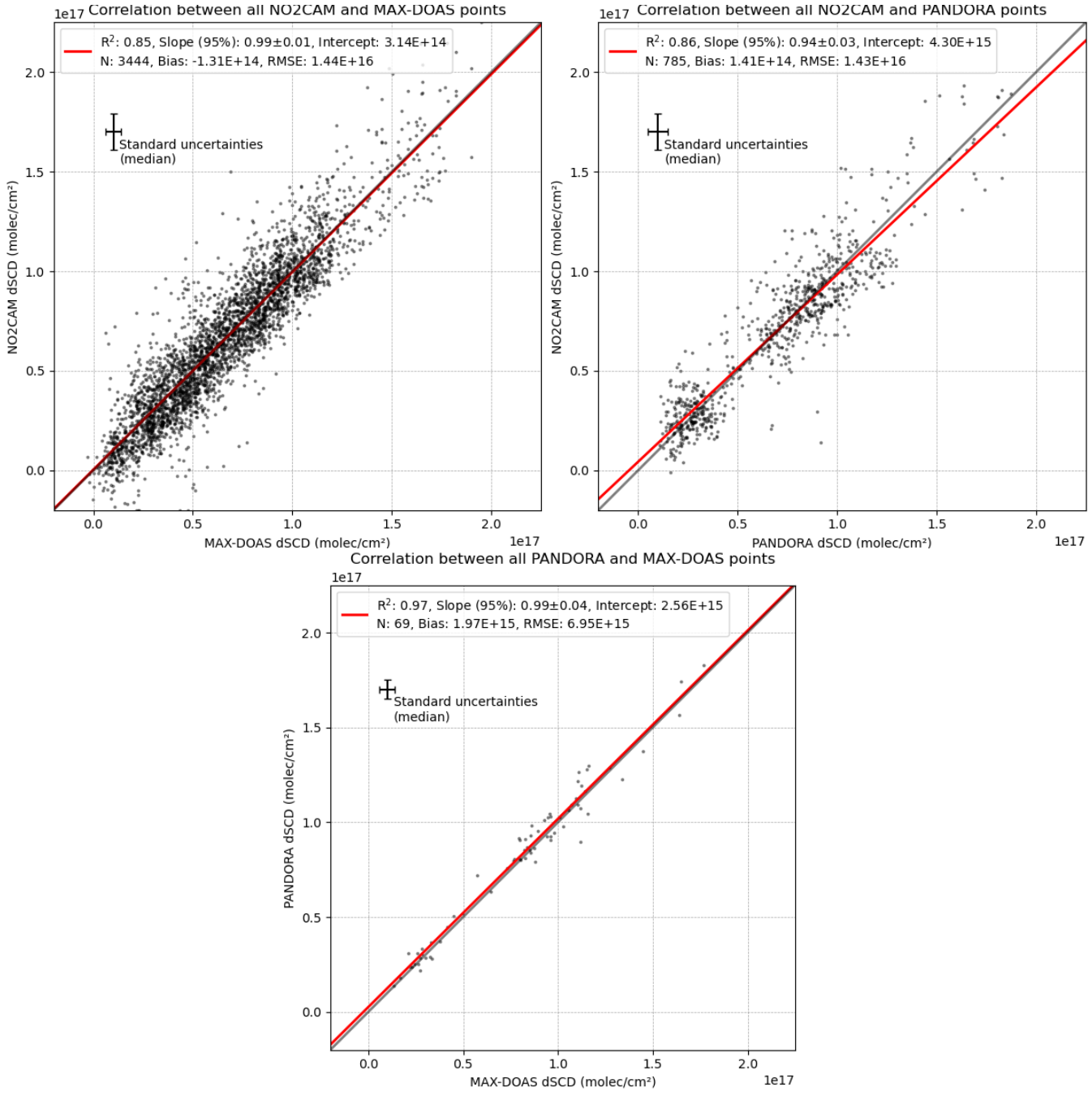

Figure 9. Scatterplots comparing the NO2 camera with the MAX-DOAS (upper left panel) and Pandora (upper right panel), including a linear regression for each. Measurement points were filtered to elevations above 1° (strictly) and time difference under 5 minutes. The lower panel shows a direct comparison of the MAX-DOAS and Pandora, using the same filters.

https://doi.org/10.5194/egusphere-2025-2255
Preprint. Discussion started: 2 June 2025

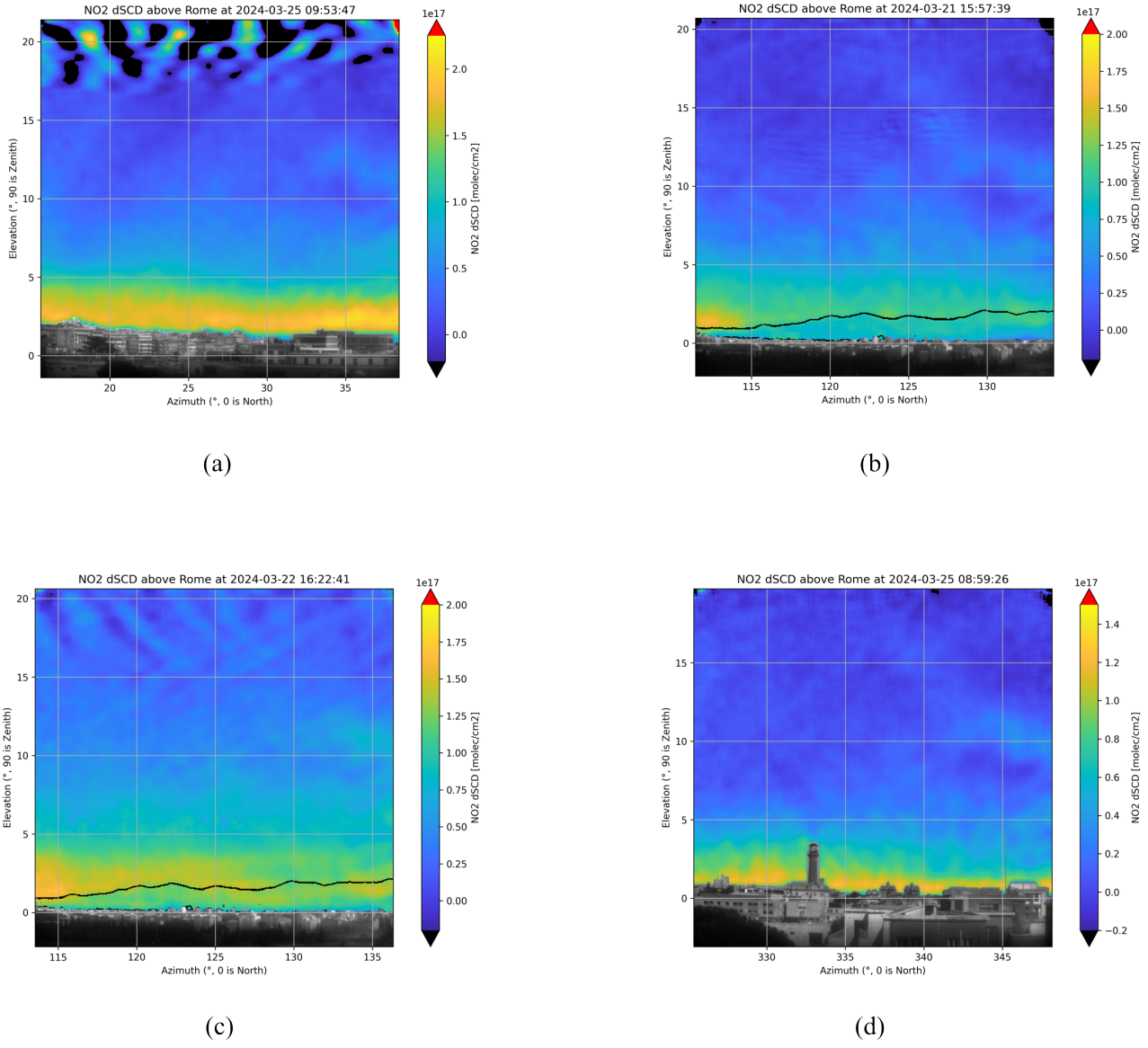

Figure 10. NO_2 dSCD maps for the four main azimuth directions in the measurement campaign. Note the different scales for the different directions. All times shown are UTC. On panes (a) and (c), the effects of moving clouds are visible at the top of the image.

https://doi.org/10.5194/egusphere-2025-2255
Preprint. Discussion started: 2 June 2025

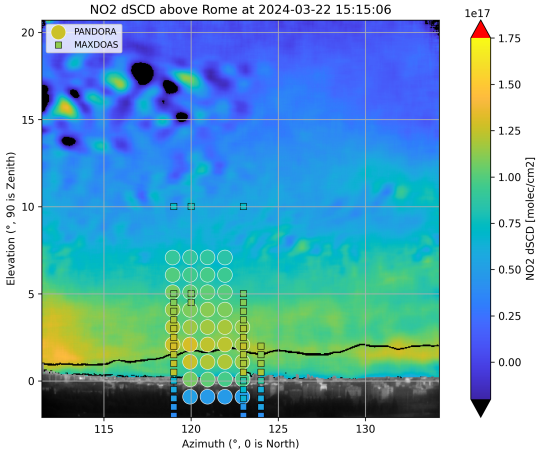

Figure 11. Qualitatively, the NO_2 dSCDs of both the Pandora and MAX-DOAS agree well with the dSCD obtained with the NO_2 camera. The size of the dots is not representative for the field of view of the instruments.

5.4 Uncertainties

Sections 3.4, 4.2.2 and 4.2.1 above have already described the methodology followed by each instrument for uncertainty estimation. Table 5 presents summary statistics on the resulting estimated errors. As already mentioned, systematic or structured uncertainties are not (yet) considered for the NO_2 camera retrievals, so we expect serious underestimation of uncertainty. As a pragmatic alternative, we also report the standard deviation of NO_2 dSCDs among all pixels from the same elevation and same cube, which we consider to be an empirical estimate of retrieval errors. This probably over-estimates the uncertainty, especially at low elevations, since it also includes the true azimuthal variation of the NO_2 field. On the other hand, the empirical indicator might under-estimate the uncertainty in case of a systematic bias. However, the comparison with the other instruments in Fig. 9 did not reveal any such bias, so we believe this empirical approach is valuable.

Instrument	Uncertainty ($\times 10^{15}$ molec/cm^2) *Median [95% coverage range]*
NO_2 camera (from shot noise)	1.3 [0.5–1.7]
NO_2 camera (empirical)	9 [4–26]
MAX-DOAS	4 [3–6]
Pandora	5 [3–10]

Table 5. Statistics on NO2 dSCD uncertainty estimates for the whole campaign for each instrument.

https://doi.org/10.5194/egusphere-2025-2255
Preprint. Discussion started: 2 June 2025

6 Conclusions

We have presented the results of an intercomparison campaign between the NO_2 camera, an AOTF-based spectral imager optimized for the measurement of NO_2 slant column densities (SCD) from the scattered solar light in the 425–455 nm domain, and two reference diffraction grating-based spectrometers: a MAX-DOAS, and a Pandora. The three instruments were deployed in March 2024 at the BAQUNIN supersite on top of the physics department building of the Sapienza university, located in the center of Rome, Italy. They were operated in such a way that the field of view of the NO_2 camera was sampled by the two other instruments at different azimuths, and under strict coincidence criteria. The focus was on the NO_2 distribution close to the horizon, where local sources and winds are shaping the NO_2 field. Given the unconventional concept of the NO_2 camera, the first and main purpose of the campaign was to validate its measured NO_2 SCDs with the coincident observations of the reference instruments. The secondary objectives were: (1) to demonstrate that the NO_2 camera hyperspectral cubes can be processed by the DOAS method, the leading technique for the processing of UV–visible light spectra; and (2) to illustrate the capabilities of the NO_2 camera in revealing the spatial and temporal gradients of an urban NO_2 field.

The primary objective was achieved through the analysis of hundreds of coincident observations, which revealed that large NO_2 dSCDs ($> 2 \times 10^{16}$ molec/cm^2) are usually well retrieved by the NO_2 camera. Those are typically found at low elevation angles, where the light crosses air masses of high NO_2 concentrations over long distances. Comparison of coincident observations with the MAX-DOAS and the Pandora for elevations up to 10° shows good agreement ($R^2 = 0.86$ for both), demonstrating that the NO_2 camera can provide meaningful quantitative information.

All of the camera acquisitions were performed in a "DOAS mode", a driving scheme in which the AOTF bandpass filter is swept by small steps (0.15 nm) across a wavelength range in order to obtain *continuous spectra*. Contrary to diffraction grating-based instruments, regularly sampling a chunk of optical spectrum with fine steps requires an excellent control of the AOTF. In general, no problem was found in applying the DOAS method, confirming the good tuning performance of the instrument. The main problems encountered were related to the stability of the shape of the AOTF response function, and to changes of illumination conditions during the acquisitions.

While capturing spatial gradients is easy for a native imaging system such as the NO_2 camera, observations of extended scenes are not routinely performed by conventional operational air quality remote sensing instruments such as the MAX-DOAS and the Pandora spectrometers. It requires the sequential pointing of the collecting optics in many pairs of azimuth and elevation angles. On the other hand, the light spectrum is captured at once. The *images*, eventually produced based on the results of the MAX-DOAS and Pandora measurements, lack details usually helpful for understanding the context of the observations or seeing fine-scale features. The $20° \times 20°$ field of view of the NO_2 camera could only be sampled by the other two instruments at the price of long acquisition sequences. The variation of the temporal coincidence criteria, between ± 5 and ± 30 minutes, highlights the temporal variability of the urban NO_2 field, be it driven by changes in the emissions, or in illumination conditions. In some scenes, local enhancements are clearly captured by the imager, revealing spatial gradients which would be hard to see with the other ground-based instruments.

https://doi.org/10.5194/egusphere-2025-2255
Preprint. Discussion started: 2 June 2025

These encouraging results are calling for further usage of the NO_2 camera. First, the few local and transient enhancements which have already been detected are just a glimpse of the many more "pollution events" that can happen in an urban environment such as Rome. Long-term installation of the instrument as part of a supersite like BAQUNIN would allow for studying these events in order to understand their origin, their amplitude, and the fate of the plume. Second, the tuning range of the instrument is not limited to 425–450 nm, such that the acquisition of spectral images in a region of strong O_4 absorption (470–480 nm) would allow for informing on the visual range of the pixel line of sight. This information will be required in order to retrieve tropospheric NO_2 columns from the NO_2 dSCD maps measured by the camera. Finally, the instrument itself can be improved further, mainly by increasing the frame-rate of the detector, better characterizing the spectral response function, and reducing the internal stray light.

Data availability. All data points from the campaign in Rome which were used in compare the NO_2 camera to the reference instruments will be published on Zenodo in May 2025 and listed at URL https://zenodo.org/communities/qa4eocalval. Given their important volume, the full-resolution data from the NO_2 camera during the campaign will *not* be included there, but are available by request to the corresponding authors.

Author contributions. PG, CB and ED developed the NO_2 camera, operated it during the campaign, processed its data, performed the instruments comparison and wrote the manuscript. DP wrote some driver software for NO_2 camera. NB, SC, ADB, PP, EC reviewed the manuscript. SC, AMI and PP operated the reference instruments and processed their data. ADB and NF provided technical and logistic support for the campaign. LDL, FC are the principal investigators of the MAX-DOAS instrument.

Competing interests. All authors declare having no competing interests.

Acknowledgements. This work was performed in the frame of the Instrument Data Quality Evaluation and Assessment Service – Quality Assurance for Earth Observation (IDEAS-QA4EO) contract funded by ESA-ESRIN (n. 4000128960/19/I-NS). We are grateful to Angelika Dehn and Philippe Goryl (ESA-ESRIN GMQ) for their invaluable support to this activity.

The SkySpec-2D system was acquired under the project “Sviluppo delle Infrastrutture e Programma Biennale degli Interventi del Consiglio Nazionale delle Ricerche—Potenziamento Infrastrutturale: progetti di ricerca strategici per l’ente. Progetto 55—ASSE CENTRO”.

The authors would like thank our colleagues Michel Van Roozendael and his team for the valuable feedback on early results and for the QDOAS software, David Bolsée and Nuno Pereira for their help obtaining the PTC curve of the detector, and the engineering department of BIRA-IASB for their support. Manuel Roca and Axel Kreuter from LuftBlick OG gave very appreciated support in the operation and data processing of the Pandora instrument. Additionally, the authors would like to thank Dimitris Karagkiozidis for making his EKO library available to them.

https://doi.org/10.5194/egusphere-2025-2255
Preprint. Discussion started: 2 June 2025

References

Cede, A., Tiefengraber, M., Gebetsberger, M., and Spinei Lind, E.: Pandonia Global Network Data Products Readme Document, LuftBlick, https://www.pandonia-global-network.org/wp-content/uploads/2025/01/PGN_DataProducts_Readme_v1-8-10.pdf, 2025.

Chance, K. and Kurucz, R.: An improved high-resolution solar reference spectrum for earth's atmosphere measurements in the ultraviolet, visible, and near infrared, Journal of Quantitative Spectroscopy and Radiative Transfer, 111, 1289–1295, https://doi.org/10.1016/j.jqsrt.2010.01.036, 2010.

Chang, I. C.: Noncollinear acousto-optic filter with large angular aperture, Applied Physics Letters, 25, 370–372, https://doi.org/10.1063/1.1655512, 1974.

Chen, X., Qi, L., Li, S., and Duan, X.: Long-term NO2 exposure and mortality: A comprehensive meta-analysis, Environmental Pollution, 341, 122 971, https://doi.org/10.1016/j.envpol.2023.122971, 2024.

De Craemer, S., Vercauteren, J., Fierens, F., Lefebvre, W., and Meysman, F. J. R.: Using Large-Scale NO2 Data from Citizen Science for Air-Quality Compliance and Policy Support, Environmental Science & Technology, 54, 11 070–11 078, https://doi.org/10.1021/acs.est.0c02436, 2020.

Dekemper, E., Loodts, N., Van Opstal, B., Maes, J., Vanhellemont, F., Mateshvili, N., Franssens, G., Pieroux, D., Bingen, C., Robert, C., De Vos, L., Aballea, L., and Fussen, D.: Tunable acousto-optic spectral imager for atmospheric composition measurements in the visible spectral domain, Appl. Opt., 51, 6259–6267, https://doi.org/10.1364/AO.51.006259, 2012.

Dekemper, E., Vanhamel, J., Van Opstal, B., and Fussen, D.: The AOTF-based NO$<sub$ >2$</$sub$ > camera, Atmospheric Measurement Techniques, 9, 6025–6034, https://doi.org/10.5194/amt-9-6025-2016, 2016.

Finkenzeller, H. and Volkamer, R.: O2–O2 CIA in the gas phase: Cross-section of weak bands, and continuum absorption between 297–500 nm, Journal of Quantitative Spectroscopy and Radiative Transfer, 279, 108 063, https://doi.org/10.1016/j.jqsrt.2021.108063, 2022.

Fussen, D., Baker, N., Debosscher, J., Dekemper, E., Demoulin, P., Errera, Q., Franssens, G., Mateshvili, N., Pereira, N., Pieroux, D., and Vanhellemont, F.: The ALTIUS atmospheric limb sounder, J. Quant. Spectrosc. Radiat. Transf., https://doi.org/10.1016/J.JQSRT.2019.06.021, publisher: Pergamon, 2019.

Harris, S. E. and Wallace, R. W.: Acousto-Optic Tunable Filter, J. Opt. Soc. Am., 59, 744, https://www.osapublishing.org/josa/abstract.cfm?id=53721, 1969.

Herman, J., Cede, A., Spinei, E., Mount, G., Tzortziou, M., and Abuhassan, N.: NO2 column amounts from ground-based Pandora and MFDOAS spectrometers using the direct-sun DOAS technique: Intercomparisons and application to OMI validation, Journal of Geophysical Research: Atmospheres, 114, https://doi.org/10.1029/2009JD011848, _eprint: https://onlinelibrary.wiley.com/doi/pdf/10.1029/2009JD011848, 2009.

Hermans, C., Vandaele, A. C., Carleer, M., Fally, S., Colin, R., Jenouvrier, A., Coquart, B., and Mérienne, M.-F.: Absorption cross-sections of atmospheric constituents: NO2, O2, and H2O, Environmental Science and Pollution Research, 6, 151–158, https://doi.org/10.1007/bf02987620, 1999.

Heue, K.-P., Wagner, T., Broccardo, S. P., Walter, D., Piketh, S. J., Ross, K. E., Beirle, S., and Platt, U.: Direct observation of two dimensional trace gas distributions with an airborne Imaging DOAS instrument, Atmospheric Chemistry and Physics, 8, 6707–6717, https://doi.org/10.5194/acp-8-6707-2008, 2008.

https://doi.org/10.5194/egusphere-2025-2255
Preprint. Discussion started: 2 June 2025

Huangfu, P. and Atkinson, R.: Long-term exposure to NO2 and O3 and all-cause and respiratory mortality: A systematic review and meta-analysis, Environment International, 144, 105 998, https://doi.org/10.1016/j.envint.2020.105998, 2020.

Iannarelli, A. M., Di Bernardino, A., Casadio, S., Bassani, C., Cacciani, M., Campanelli, M., Casasanta, G., Cadau, E., Diémoz, H., Mevi, G., Siani, A. M., Cardaci, M., Dehn, A., and Goryl, P.: The Boundary Layer Air Quality-Analysis Using Network of Instruments (BAQUNIN) Supersite for Atmospheric Research and Satellite Validation over Rome Area, Bulletin of the American Meteorological Society, 103, E599–E618, https://doi.org/10.1175/bams-d-21-0099.1, 2022.

Janesick, J. R.: Photon transfer, no. PM170 in SPIE Press monograph, SPIE, Bellingham, Wash. <1000 20th St. Bellingham WA 98225-6705 USA>, ISBN 9780819478382, restricted to subscribers or individual electronic text purchasers, 2007.

Last, J. A., Sun, W. M., and Witschi, H.: Ozone, NO, and NO2: oxidant air pollutants and more., Environmental Health Perspectives, 102, 179–184, https://doi.org/10.1289/ehp.94102s10179, 1994.

Lauriks, F., Jacobs, D., and Meysman, F.: CurieuzenAir: Data collection, data analysis and results, Tech. rep., Universiteit Antwerpen, 2022.

Lohberger, F., Hönninger, G., and Platt, U.: Ground-based imaging differential optical absorption spectroscopy of atmospheric gases, Applied Optics, 43, 4711, https://doi.org/10.1364/ao.43.004711, 2004.

Merlaud, A., Belegante, L., Constantin, D.-E., Den Hoed, M., Meier, A. C., Allaart, M., Ardelean, M., Arseni, M., Bösch, T., Brenot, H., Calcan, A., Dekemper, E., Donner, S., Dörner, S., Balanica Dragomir, M. C., Georgescu, L., Nemuc, A., Nicolae, D., Pinardi, G., Richter, A., Rosu, A., Ruhtz, T., Schönhardt, A., Schuettemeyer, D., Shaiganfar, R., Stebel, K., Tack, F., Nicolae Vâjâiac, S., Vasilescu, J., Vanhamel, J., Wagner, T., and Van Roozendael, M.: Satellite validation strategy assessments based on the AROMAT campaigns, Atmos. Meas. Tech., 13, 5513–5535, https://doi.org/10.5194/amt-13-5513-2020, 2020.

Mettepenningen, G., Fayt, C., Tack, F., Van Doorne, C., Bogaert, P., Jacobs, L., Berkenbosch, S., Aubry, A., Desmet, F., Robert, C., De Mazière, M., and Van Roozendael, M.: UV-Vis remote sensing of atmospheric pollutants from a wind turbine platform in the North Sea: the SEMPAS project, in: EGU General Assembly 2024, Copernicus GmbH, Vienna, Austria, https://doi.org/10.5194/egusphere-egu24-11955, 2024.

Morrow, P. E.: Toxicological data on NOx: An overview, Journal of Toxicology and Environmental Health, 13, 205–227, https://doi.org/10.1080/15287398409530494, 1984.

Peters, E., Ostendorf, M., Bösch, T., Seyler, A., Schönhardt, A., Schreier, S. F., Henzing, J. S., Wittrock, F., Richter, A., Vrekoussis, M., and Burrows, J. P.: Full-azimuthal imaging-DOAS observations of NO_2 and O_4 during CINDI-2, Atmospheric Measurement Techniques, 12, 4171–4190, https://doi.org/10.5194/amt-12-4171-2019, 2019.

Pettinari, P., Castelli, E., Papandrea, E., Busetto, M., Valeri, M., and Dinelli, B. M.: Towards a New MAX-DOAS Measurement Site in the Po Valley: NO2 Total VCDs, Remote Sensing, 14, 3881, https://doi.org/10.3390/rs14163881, 2022.

Platt, U. and Stutz, J.: Differential optical absorption spectroscopy, Physics of Earth and Space Environments, Springer Berlin Heidelberg, Berlin, [Germany] ;, ISBN 9783540757764, https://doi.org/10.1007/978-3-540-75776-4, includes bibliographical references at the end of each chapters and index. Description based on print version record. "With 272 Figures and 55 Tables.", 2008.

Platt, U., Lübcke, P., Kuhn, J., Bobrowski, N., Prata, F., Burton, M., and Kern, C.: Quantitative imaging of volcanic plumes - Results, needs, and future trends, J. Volcanol. Geotherm. Res., 300, 7–21, https://doi.org/10.1016/j.jvolgeores.2014.10.006, publisher: Elsevier B.V., 2014.

Rothman, L., Gordon, I., Babikov, Y., Barbe, A., Chris Benner, D., Bernath, P., Birk, M., Bizzocchi, L., Boudon, V., Brown, L., Campargue, A., Chance, K., Cohen, E., Coudert, L., Devi, V., Drouin, B., Fayt, A., Flaud, J.-M., Gamache, R., Harrison, J., Hartmann, J.-M., Hill, C., Hodges, J., Jacquemart, D., Jolly, A., Lamouroux, J., Le Roy, R., Li, G., Long, D., Lyulin, O., Mackie, C., Massie, S., Mikhailenko, S.,

https://doi.org/10.5194/egusphere-2025-2255
Preprint. Discussion started: 2 June 2025

Müller, H., Naumenko, O., Nikitin, A., Orphal, J., Perevalov, V., Perrin, A., Polovtseva, E., Richard, C., Smith, M., Starikova, E., Sung, K., Tashkun, S., Tennyson, J., Toon, G., Tyuterev, V., and Wagner, G.: The HITRAN2012 molecular spectroscopic database, Journal of Quantitative Spectroscopy and Radiative Transfer, 130, 4–50, https://doi.org/10.1016/j.jqsrt.2013.07.002, 2013.

Seinfeld, J. H. and Pandis, S. N.: Atmospheric chemistry and physics, J. Wiley, Hoboken, N.J, 2nd ed (online-ausg.) edn., ISBN 9780471720188, 2006.

Serdyuchenko, A., Gorshelev, V., Weber, M., Chehade, W., and Burrows, J. P.: High spectral resolution ozone absorption cross-sections – Part 2: Temperature dependence, Atmospheric Measurement Techniques, 7, 625–636, https://doi.org/10.5194/amt-7-625-2014, 2014.

Suhre, D. R., Denes, L. J., and Gupta, N.: Telecentric confocal optics for aberration correction of acousto-optic tunable filters, Appl. Opt., 43, 1255, https://doi.org/10.1364/AO.43.001255, publisher: Optical Society of America, 2004.

Thalman, R. and Volkamer, R.: Temperature dependent absorption cross-sections of O2–O2 collision pairs between 340 and 630 nm and at atmospherically relevant pressure, Physical Chemistry Chemical Physics, 15, 15 371, https://doi.org/10.1039/c3cp50968k, 2013.

Van Roozendael, M., Hendrick, F., Friedrich, M. M., Fayt, C., Bais, A., Beirle, S., Bösch, T., Navarro Comas, M., Friess, U., Karagkiozidis, D., Kreher, K., Merlaud, A., Pinardi, G., Piters, A., Prados-Roman, C., Puentedura, O., Reischmann, L., Richter, A., Tirpitz, J.-L., Wagner, T., Yela, M., and Ziegler, S.: Fiducial Reference Measurements for Air Quality Monitoring Using Ground-Based MAX-DOAS Instruments (FRM4DOAS), Remote Sensing, 16, https://doi.org/10.3390/rs16234523, 2024.

Vandaele, A., Hermans, C., Simon, P., Carleer, M., Colin, R., Fally, S., Mérienne, M., Jenouvrier, A., and Coquart, B.: Measurements of the NO2 absorption cross-section from 42 000 cm-1 to 10 000 cm-1 (238–1000 nm) at 220 K and 294 K, Journal of Quantitative Spectroscopy and Radiative Transfer, 59, 171–184, https://doi.org/10.1016/s0022-4073(97)00168-4, 1998.

Voloshinov, V. B., Yushkov, K. B., and Linde, B. B. J.: Improvement in performance of a TeO2 acousto-optic imaging spectrometer, J. Opt. A Pure Appl. Opt., 9, 341–347, https://doi.org/10.1088/1464-4258/9/4/006, 2007.

Wagner, T., Beirle, S., and Deutschmann, T.: Three-dimensional simulation of the Ring effect in observations of scattered sun light using Monte Carlo radiative transfer models, Atmospheric Measurement Techniques, 2, 113–124, https://doi.org/10.5194/amt-2-113-2009, 2009.

World Health Organization: WHO Global Air Quality Guidelines. Particulate matter (PM2.5 and PM10), ozone, nitrogen dioxide, sulfur dioxide and carbon monoxide, WHO, Geneva, ISBN 978-92-4-003422-8, 2021.